Model of Microphase Separation in Two-Dimensional Gels

Orit Peleg,[†] Martin Kröger,[‡] and Yitzhak Rabin*[,§]

Department of Physics, Bar-Ilan University, Ramat-Gan 52900, Israel; Polymer Physics, ETH Zürich, Department of Materials, Wolfgang-Pauli-Str. 10, CH-8093 Zürich, Switzerland; and Department of Physics, Nano-materials Research Center, Institute of Nanotechnology and Advanced Materials, Bar-Ilan University, Ramat-Gan 52900, Israel

Received December 7, 2007; Revised Manuscript Received February 5, 2008

ABSTRACT: We have recently introduced a simple model which contains the basic features of phase separation in cross-linked polymer gels: a stretched elastic network of Lennard-Jones particles [Peleg, O.; et al. *EPL* **2007**, 77, 58007]. While the original work clearly demonstrated the phenomenology of the model at a limited set of system parameters, this paper explores quantitative details and gives answers to many of the questions which remained open. We define and analyze an order parameter, explore the phase diagram, and identify the range of elastic constants in which microphase separation is observed and analyze the microphase separation patterns. We discuss the microscopic origin of the formation of linear rather than globular filaments as well as monitor and quantify the reorganization of the network, not only in equilibrium but also its dynamics upon applying a shear deformation. These simulations provide us with the elastic properties, most importantly, the shear modulus, whose magnitude is shown to correlate with the order parameter.

I. Introduction

The volume phase transition in polymer networks (gels) is accompanied by a phenomenon called phase separation.[1,2] When a polymer network swollen by solvent is brought (e.g., by changing the temperature) to poor solvent conditions, deswelling takes place and the gel shrinks. Since the process of deswelling is controlled by slow diffusion of the solvent molecules out of the gel, its duration depends crucially on the dimensions of the gel. For small (say 10 μm) gels, the process of deswelling is instantaneous (on order of a second), and one can approximate it as a uniform change of concentration. If, however, the gel is macroscopic (1 cm), it will change its total volume slowly, in a process that may take days and weeks. However, since diffusion on length scales comparable to the wavelength of light is nearly instantaneous, domains of high and low polymer concentration form inside the gel almost immediately following the temperature quench, light scattering increases, and the gel becomes opaque. This phase transition behavior of large gels in which the change of total volume and phase separation on microscopic and mesoscopic scales are well separated in time is the motivation for the present study of phase separation in polymer networks at fixed volume.

The fact that a gel is a connected network permeated by solvent imposes severe constraints on the reorganization of its constituents during the process of phase separation and the resulting formation of domains of high and of low polymer concentration. In particular, the formation of truly macroscopic dilute domains is suppressed by the connectivity of the network, and only microphase separation is possible under constant volume conditions. The presence of network constraints is the source of the difference between phase separation in gels and in binary liquid mixtures where macrophase separation (between, e.g., oil and water) is observed. Thus, even though the equilibrium properties of phase separation in binary liquid mixtures are well understood (its critical behavior belongs to the same universality class as the Ising model[3]), the results cannot be directly extrapolated to model equilibrium phase separation in gels. The difference between liquid mixtures and gels applies to dynamics of phase separation as well. Thus, in liquid mixtures (of either small molecules or polymers; see ref 4), depending on whether the system was brought to the metastable or the unstable region of the phase diagram, phase separation takes place via nucleation or spinodal decomposition, respectively.[5,6] While there have been several attempts to construct kinetic models of phase separation in gels, based on phenomenological expressions for the free energy,[7,8] the present understanding of the physical mechanisms that drive phase separation in gels lags behind that of liquid mixtures. Our goal in the present work is to provide an intuitive picture of the equilibrium and kinetics of phase separation in connected networks. We introduce a simple model that does not attempt to capture many of the properties of real gels; instead, it deals with the essence of the problem—the interplay between driving (attractive) and opposing (elastic) forces in the presence of constraints (permanent cross-links). To this end, we use the molecular dynamics approach to reach and identify the final steady states of the network. We characterize the mesoscopic spatial patterns that arise during the transition, study the kinetics of their formation, and investigate the mechanical properties of the resulting, highly microscopically inhomogeneous, microphase-separated gel.

Section II motivates and defines the model. Section III presents results. We will offer evidence that the observed mesoscopic patterns are a quite general feature of phase separation in a connected network and will obtain some insight about their properties and the mechanism of their formation. We will deal with all aspects mentioned in the abstract. Section IV provides conclusions and outlook.

II. The Model

Our "minimal" model builds on a two-dimensional network, comprised of N particles. Each particle of mass m (representing a "node" in the network) is connected through identical harmonic springs with spring coefficient k to a fixed number of particles, precisely those which were its nearest neighbors in the initial configuration. Similarly to the phantom chain model of polymer networks,[9] the springs are not endowed with physical attributes such as mass or excluded volume. Even though the present model is motivated by polymer gels which possess entropic

* Corresponding author. E-mail: rabin@mail.biu.ac.il.
[†] Department of Physics, Bar-Ilan University.
[‡] ETH Zürich.
[§] Department of Physics, Nano-materials Research Center, Institute of Nanotechnology and Advanced Materials, Bar-Ilan University.

10.1021/ma702732t CCC: $40.75
Published on Web 04/15/2008

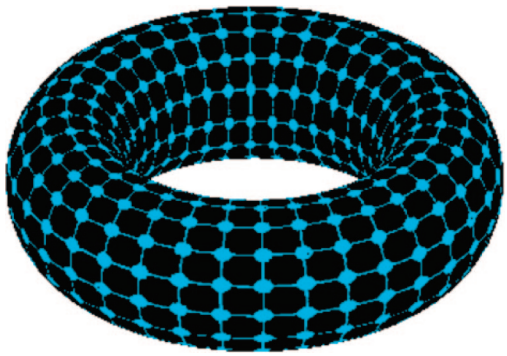

Figure 1. Simple cubic torus. Lines and nodes represent springs and Lennard-Jones (LJ) particles, respectively. The harmonic springs have spring coefficient k and extension l_0 in the shown configuration, which is topologically equivalent to the investigated system with periodic boundary conditions.

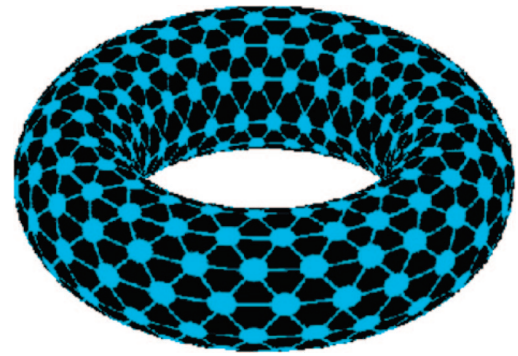

Figure 2. Same as Figure 1 for the hexagonal lattice torus.

elasticity, in this work we neglect any temperature dependence of the spring constant k. We would like to stress that our model should not be considered as a coarse-grained model of a gel; rather, it is a toy model which contains what we believe to be the essential physical attributes of polymer networks. Since many properties of real gels are neglected, the relevance of our results to real gels can be decided upon only a posteriori, by comparing them to experimental results. In addition to the spring forces, we introduce attractive interactions by having all the particles interact via the Lennard-Jones (LJ) potential $U_{LJ}(r_{ij}) = 4\epsilon[(\sigma/r_{ij})^{12} - (\sigma/r_{ij})^6]$, where $r_{ij} \equiv |\mathbf{r}_i - \mathbf{r}_j|$ is the relative distance between particles i and j. The minimum of the potential is located at $r_{min} = 2^{1/6}$; the potential is shifted by a constant such that $U_{LJ}(r_{cut}) = 0$ where $r_{cut} = 3 \times 2^{1/6}$; we use the velocity Verlet algorithm[10] with integration time step $\Delta t = 0.004$ to integrate Newton's equation of motion. We prefer to report the number of integration time steps rather than LJ time units; 1M steps correspond to 4000 LJ units.

We here choose the initial state to be a simple square (or alternatively, a hexagonal) $\sqrt{N} \times \sqrt{N}$ grid with lattice spacing l_0, where four (six) nearest neighbors are assigned to each particle. The velocities of the particles are initialized with vectors of random direction and of a $\sqrt{2T}$ magnitude, where T is the temperature. The system is studied by molecular dynamics simulations in the (N, V, T) ensemble, where V is total area of the system.

Throughout this paper we use dimensionless LJ units[10–12] which are defined by choosing σ, m, and ϵ to be the units of length, mass, and energy, respectively, and making the replacements $r \rightarrow r\sigma$ (length), $e \rightarrow e\epsilon$ (energy), and $t \rightarrow t\sqrt{m\sigma^2/\epsilon}$. The temperature is kept constant by rescaling the velocities each 200 steps to agree with the equipartiton principle[10] as described by algorithm 1, (cf. Appendix B), where $v[i]_x$ and $v[i]_y$ are the x- and y-components, respectively, of the velocity of particle number i.

The system is subject to periodic boundary conditions (PBC) in the x- and y-directions, i.e. wrapped around an infinitely large torus (see Figure 1 for the square grid and Figure 2 for the hexagonal grid). Because of the periodic boundary conditions, the harmonic springs remain (at least on average) stretched, and their presence makes the network behave as an elastic solid. After every integration step, the new coordinates are checked to agree with the boundary conditions as described by algorithm 2, where L_x and L_y denote the system sizes along x and y directions, respectively.

When calculating the energy of the springs (E_{SP}), we take under consideration the PBC as described by algorithm 3, where ζ is half-the number of nearest neighbors (2 for a simple cubic lattice and 3 for a hexagonal lattice). In this strategy a spring of length which is bigger than half the system size is always converted to a spring of length which is smaller than the system size. This is why the system size and the k value are chosen large enough to avoid the relative displacement of any pair of particles beyond half the box size.

With the present choices of $l_0 = 3.5$, $N = 10\,000$ or $N = 250\,000$, $k \in [1/1000, 1/2]$ for the square grid, and $k \in [1/1500, 1/3]$ for the hexagonal grid, the systems can be equilibrated within accessible simulation times (kinetic barriers to structural reorganization increase with spring stiffness and with temperature raising) for a sufficiently broad range of temperatures above T_{min}, and a steady state is reached in the sense that all monitored parameters in the system (e.g., the total number of particles and the total energy of each of the phases) do not change in time, apart from small fluctuations about their mean values.

III. Results

A. Order Parameter and Phase Diagram. We introduce a length scale $r_{cluster}$ such that particles with separations less than $r_{cluster}$ are considered to belong to the same cluster (we chose $r_{min} < r_{cluster} = 1.5 < r_{cut}$), as in ref 13. In order to study phase separation in the system, we distinguish between a high-density phase (HDP) and a low-density phase (LDP) such that a particle which belongs to a cluster is considered as a HDP particle and one which does not belong to a cluster is a LDP particle. We will present snapshots of the instantaneous configuration in which we use the following coloring code: HDP and LDP particles are shown as green and blue points, respectively; the springs connecting LDP particles are shown as blue lines, those connecting particles in the same cluster are shown as green lines, and those connecting particles from different clusters or connecting particles belonging to HDP and LDP are shown as orange lines. Initially, the particles are placed at the nodes of a grid and given random velocities (corresponding to some sufficiently high temperature T_0). They fluctuate around their initial locations with amplitude proportional to $\sqrt{2T_0}$. After the system reaches equilibrium (see Figure 3), the temperature is set to a desired value, and the velocities of the particles are rescaled by algorithm 1. However, since we found that the results reported below do not depend on the initial state of the system (as long as it is not trapped in a metastable state), we skipped the initial equilibration at the higher temperature and carried out the temperature quench by placing the particles on the sites of a regular lattice and giving them random initial velocities such that the mean kinetic energy per particle corresponds to the desired final temperature T.

We define an order parameter, ϕ, as follows:

$$\phi \equiv \frac{N_{HDP}}{N} \tag{1}$$

where N_{HDP} is the number of HDP particles. The current choice of the order parameter slightly differs from the previous choice

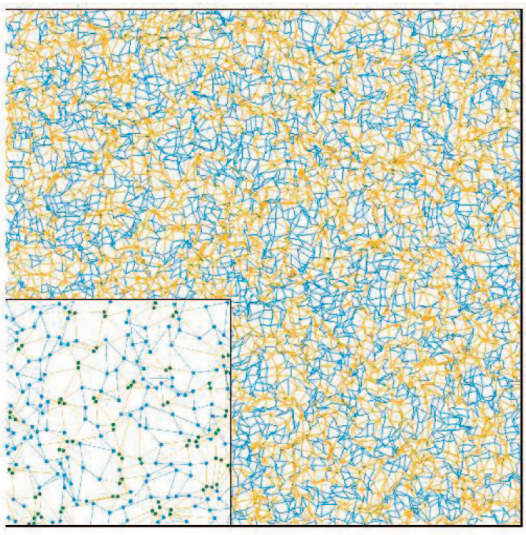

Figure 3. Snapshot of a homogeneous state of a system (relaxed from the initial square grid; cf. Figure 1) with parameters $k = 0.1$, $T = 0.9 > T^*$ (0.432). A close-up is shown in the inset. Color code is described in the first paragraph of section III.

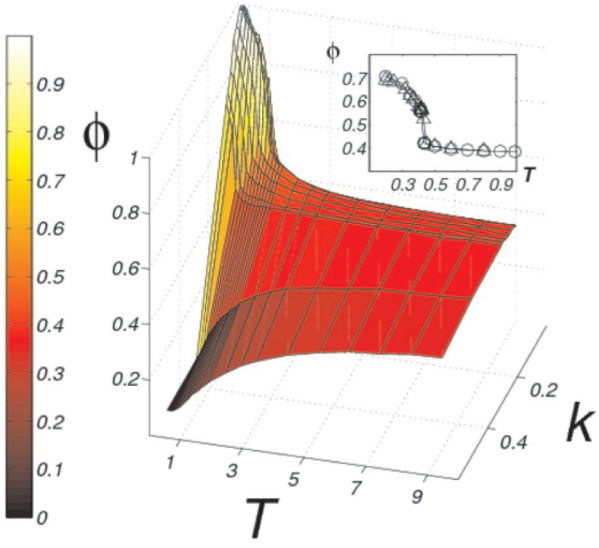

Figure 4. Phase diagram of a system with parameters $l_0 = 3.5$, N = 10 000 (result for the simple cubic lattice; cf. Figure 1). At the inset, a plot of ϕ (of systems with parameters $l_0 = 3.5$, $k = 0.1$) is presented for two different system sizes, $N = 10\,000$ (○) and $N = 25\,000$ (△).

made by the authors,[13] $S \equiv N_{bc}/N$, where N_{bc} is the number of particles that belong to the biggest (percolating) cluster in the system. The order parameter ϕ usually saturates after a small number of simulation steps (<1M steps) while S saturates only after more than 10M steps.

Examination of the "phase diagram" (plot of the order parameter in (k, T) space in Figure 4 of a system with parameters $l_0 = 3.5$, N = 10^4 shows that the order parameter reaches a plateau value at high temperatures. This plateau corresponds to a macroscopically homogeneous state in which only isolated particles and small clusters of size $n \lesssim 15$ that break up and re-form continuously are observed (a snapshot of a system with $T = 0.9$ is shown in Figure 3). The plateau value of the order parameter, $\phi \sim 0.35$, is slightly below the value ~0.43 obtained for an ideal gas of noninteracting particles at the same concentration. The number of particles in clusters is lower than that corresponding to ideal gas (where "clusters" still exist according to our definition) because of the short-range repulsive

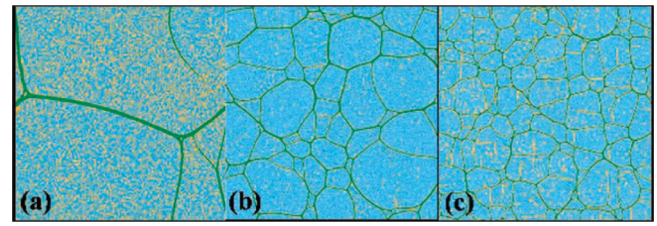

Figure 5. Typical snapshots of the steady-state patterns for a system with $k = 0.1$, $N = 250\,000$ (relaxed from the initial square grid; cf. Figure 1): (a) $T = 0.41$, (b) $T = 0.35$, (c) $T = 0.25$.

part of the LJ potential which dominates at high temperatures. We introduce the temperature $T^*(k)$ (for $T < T^*(k)$, ϕ is above the plateau value) such that for temperatures below T^* dense domains appear, and the system transforms from a homogeneous single-phase state to an inhomogeneous two-phase state. This process corresponds to microphase separation in the sense that while such domains percolate through the system, at least one of their dimensions is microscopic (independent of system size). The exact number of steps until the phase separation occurs is temperature and spring coefficient dependent (its dynamics will be discussed later on in this work). In order to check whether the phase diagram is affected by finite size effects, in the inset to Figure 4 we plotted the order parameter as a function of temperature for $k = 0.1$, for small ($N = 10\,000$) and large ($N = 250\,000$) systems. Within our accuracy, the results are indistinguishable, demonstrating that the finite size effects are negligible for the chosen system sizes.

In order to describe the region of the phase diagram in which *microphase separation* is observed, we introduce two limiting k values: k_{max} and k_{min}. According to the strategy of algorithm 3, the k_{min} bound was introduced to ensure that the relative displacement of any pair of particles does not reach half the simulation box size. The upper bound k_{max} is estimated to be ~0.31 (for simple cubic lattice) by equating the LJ energy gain for bringing two adjacent lines of particles parallel to the y-axis close together to the elastic energy loss due to uniform stretching of the rest of the network along the x-axis (assuming that this is the lowest-energy elastic-deformation mode; see a detailed estimation in Appendix A). In the region $k > k_{max}$, spring forces overcome the attractive LJ forces between the particles and suppress phase separation. Our simulations show that $0.1 < k_{max} < 0.3$, in agreement with the above analytical estimation.

Finally, we would like to stress that Figure 4 describes the behavior of the system that was initially prepared in a high-temperature state and was allowed to reach local equilibrium that corresponds to a local (but not necessarily global) free energy minimum. Therefore, T^* should be interpreted as the stability limit of the initial high temperature phase; the true equilibrium transition temperature cannot be determined by our molecular dynamics simulations and lies somewhere between T^* and T^{**} where the latter temperature is the stability limit of the low-temperature two-phase state (the corresponding hysteresis is studied in ref 13).

B. Microphase Separation Structures. We define the region where $k_{min} < k < k_{max}$ as the *microphase separation region*. In this region, $T^*(k)$ is a decreasing function of k and the order parameter ϕ increases sharply with decreasing k and T, until it reaches the value of almost unity; i.e., almost nearly all particles belong to the HDP (see Figure 4). For temperatures below $T^*(k)$, HDP structures are formed. Some of the typical structures will be described at the following paragraphs.

When a system with $k = 0.1$ is subjected to a temperature quench just below $T^* = 0.432$, a single large cluster that has the geometry of a hexagon appears in the simulation box (Figure 5a). We notice that the value $T^* = 0.432$ is below the value

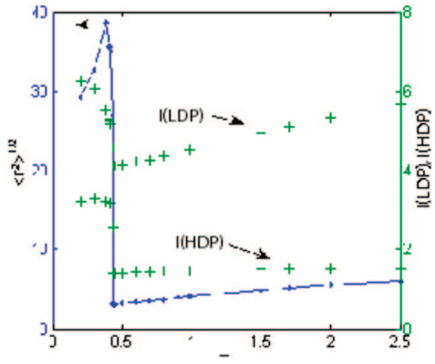

Figure 6. Plot of the root-mean-square displacement of the particles from their initial positions vs T (●) and the average spring extension, l, in the LDP and HDP (+). The data presented were evaluated for systems with parameters $N = 10\,000$, $k = 0.1$ (relaxed from the initial square grid).

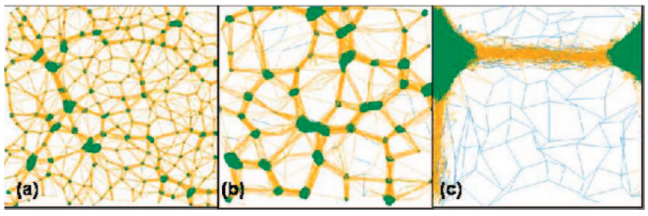

Figure 7. Typical snapshots of the steady-state patterns for a system with $k = 0.001$, $N = 10\,000$ (relaxed from the initial square grid): (a) $T = 0.2$, (b) $T = 0.3$, (c) $T = 0.5$.

0.5 of an ideal LJ gas system (which differs from our system in its lack of springs) and give the following intuitive explanation: it may appear that the loss of entropy induced by the presence of springs may cause an increase of T^* compared to T^* of a system of disconnected particles. However, the interplay between this entropic effect and the fact that the springs tend to oppose condensation (since the formation of a condensed nucleus must be accompanied by the stretching of the surrounding network and hence increases the elastic energy) reduces T^* to a lower value, the one specified above.

When the system is further cooled, several filaments grow simultaneously and collide, yielding combinations of irregular hexagons and rectangles connected by triangular vertices (Figure 5b,c), and at $T = 0.2$ percolation does not occur; there are only small clusters accompanied by slightly denser areas than the LDP, in the shape of straight lines (not shown). At this temperature the systems tend to fall into a local free energy minimum, and no steady state is reached after ~100M simulation steps.

A measure of the reorganization of the network during the process of phase separation is the root-mean-square displacement of the particles from their initial positions. In Figure 6 we plot this quantity as a function of T. The displacement increases dramatically across T^*, from a value comparable to the initial separation between particles (l_0) above T^* to about one-tenth of the system size below it. This "macroscopic" rearrangement of the network is driven by condensation of a finite fraction of particles into a percolating high-density cluster (PHDC) which occupies only a small part of the total area of the system. As a consequence of network connectivity, the remaining particles are pulled away from each other, and the average spring extension, l, in the LDP increases sharply (Figure 6). Counterintuitively, below T^*, the average spring extension in the HDP is significantly higher than $r_{min} = 2^{1/6}$ (approximately the average distance between the HDP particles); i.e., the LJ interactions occur mostly between particles that are not connected through springs.

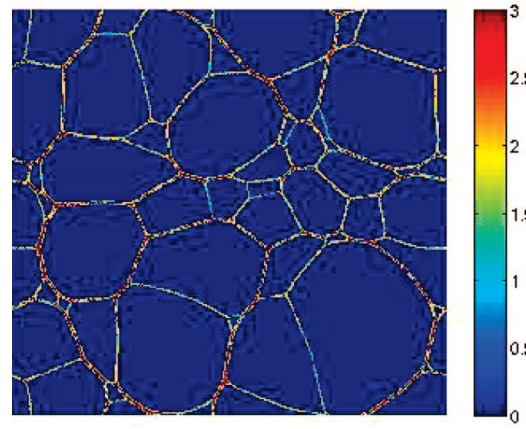

Figure 8. Snapshot of the "coarse-grained" (cf. algorithm 4) steady-state pattern (a sparse, connected graph with clustering coefficient close to unity using the notation in ref 15) for a system with parameters $N = 250\,000$, $k = 0.1$, $T = 0.35$, relaxed from the initial square grid.

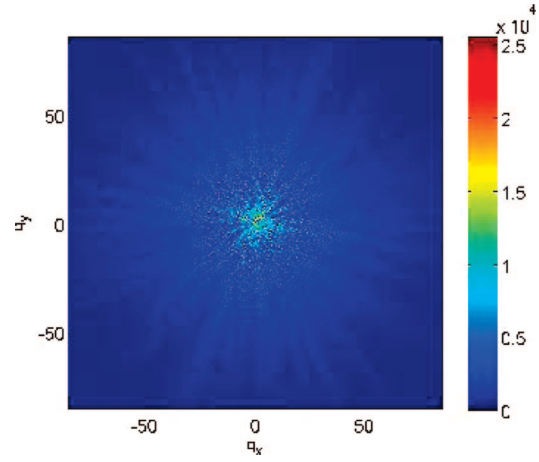

Figure 9. 2D FFT of the smoothed steady-state patterns for the snapshot shown in Figure 8. Wavenumbers are given in LJu.[11]

For weaker spring coefficients such as $k = 0.001$, at low temperatures $0.1 < T < T^*$, the typical clusters are droplet-like (opposed to the linear filaments for $k = 0.1$) as a result of the LJ force dominance over the spring forces. The average radius of the clusters increases with temperature (see for example Figure 7a,b), and eventually a single large cluster appears (Figure 7c). Unlike the spherical shape of the LJ cluster which minimizes its surface energy in the absence of springs, the diamond-like shape of this cluster is the result of minimizing the energy of stretched springs by collecting most of them into linear bundles that are stretched along the shortest paths (i.e., geodesics) along the torus. Since the stress is concentrated along the bundles, it deforms the dense cluster which assumes the shape of a diamond oriented along the principal axes of the torus.

Finally, even though this is not obvious from comparing parts b and c of Figure 7, inspection of the phase diagram (Figure 4) shows that the value of ϕ at $T = 0.3$ (Figure 7b) is higher than at $T = 0.5$. The reason is that in the latter case there is a small but finite fraction of particles which belong to the LDP (there are no isolated particles at $T = 0.3$).

C. Mesh Size and Critical Behavior. In order to define the particle density $C(\mathbf{r},t)$, the simulation box is divided into a square mesh of $N_x \times N_y$ cells. The value of $C(\mathbf{r}_{cell},t)$, defined on this mesh, is the "smoothed" number of particles which are located at a cell with coordinates $\mathbf{r}_{cell} = (n_x/L_x, n_y/L_y)$, at time t (see algorithm 4). We then perform the discrete Fourier transform

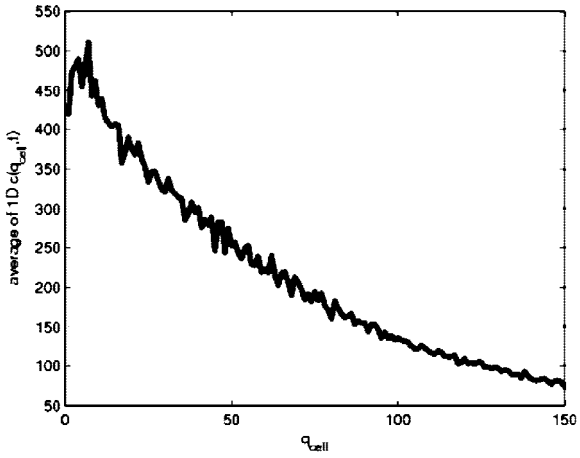

Figure 10. Average 1D FFT (at the y direction) of the smoothed steady-state patterns for a system with parameters $N = 250\,000$, $k = 0.1$, $T = 0.35$ (relaxed from the initial square grid).

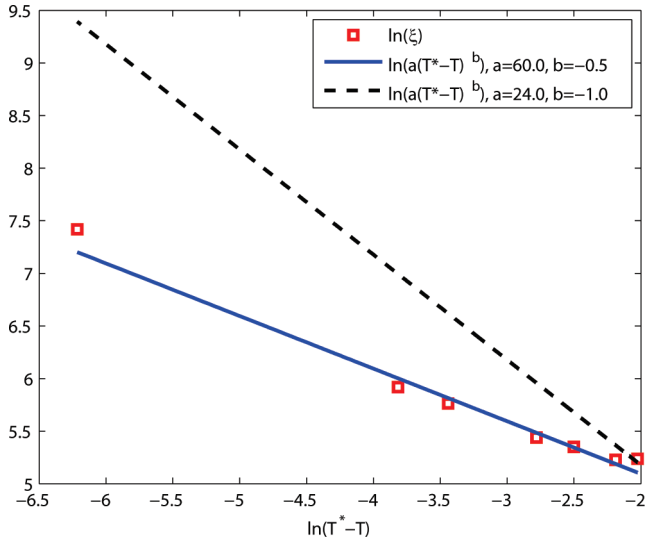

Figure 11. Characteristic length scale of cells (double-logarithmic scale).

$$c(\mathbf{q}^{\text{cell}}, t) = \sum_{n_x=0}^{N_x-1} \sum_{n_y=0}^{N_y-1} e^{-i\mathbf{q}^{\text{cell}} \cdot \mathbf{r}_{\text{cell}}} C(\mathbf{r}_{\text{cell}}, t) \tag{2}$$

where $\mathbf{q}^{\text{cell}}$ is the discrete wave vector, and evaluate eq 2 by using a fast Fourier transform (FFT) algorithm.[14] In Figure 9, we plot $c(\mathbf{q}^{\text{cell}},t)$ as a function of $\mathbf{q}^{\text{cell}}$ for a system with parameters $N = 250\,000$, $T = 0.35$, $k = 0.1$, after 3M steps, with the resolution $N_x = N_y = 1000$ for the density matrix.

In the *microphase separation region* the network separates into regions that consist of dense domains of filaments connected by 3-fold vertices. The distribution of mesh sizes of the network of filaments fluctuates about some typical value which depends on T and k and can be extracted from $c(\mathbf{q}^{\text{cell}},t)$. In principle, this can be done by angular averaging of the resulting Fourier transform of the density profile. However, since $c(\mathbf{q}_{\text{cell}},t)$is strongly anisotropic (see Figure 9), such averaging results in loss of information. In order to bypass this problem, we divide the 2D pattern (in Figure 8) into narrow slices (for example, parallel to the y-axis), apply 1D FFT to the density profile in each slice, and finally average the results over different slices. The resulting averaged 1D Fourier transform of the density profile is plotted in Figure 10. The wavenumber q^* corresponding to the peak in the density profile defines the characteristic mesh size $\xi = 2\pi/q^*$.

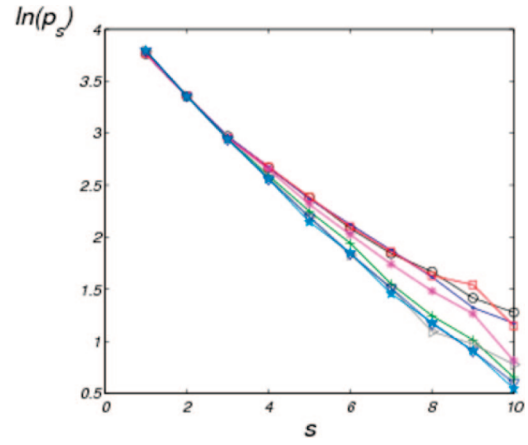

Figure 12. Natural logarithm of the number of particles p_s in clusters of given size s (including individual particles, $s = 1$) for $T = 0.434$ (○), $T = 0.435$ (●), $T = 0.44$ (□), $T = 0.5$ (∗), $T = 0.7$ (+), $T = 0.9$ (△), $T = 1.5$ (▽), and $T = 2.0$ (★). The distribution is monoexponential in the shown regime of small cluster sizes (square lattice, $N = 10\,000$, $k = 0.1$).

In Figure 11, we present results for the typical mesh size on a double-logarithmic scale for several temperatures and for systems with parameters $N = 250\,000$, $k = 0.1$. The results are well represented by the function

$$\xi \sim \frac{1}{(T^* - T)^{\nu}} \tag{3}$$

While the exact value of ν is not evaluated in this work due to lack of sufficient data near T^*, it can be seen in Figure 11 that the observed exponent, ν, is very close to the mean-field exponent ($\nu = 0.5$) but far from the exact exponent for the 2D Ising model ($\nu = 1$). We suggest that the reason may be that elasticity introduces long-range interaction, and such long-range interactions are known to suppress fluctuations and yield classical exponents.

D. Cluster Size Distribution. Focusing on a temperature series of systems with $k = 0.1$, we notice that as temperature T decreases, the probability for a particle to belong to a small cluster drops sharply from a value exceeding 0.5 to less than 0.1 at T^* and approaches zero at lower T.[13] A much smaller drop at T^* is observed for the probability to observe an isolated particle. For temperatures above T^*, the histogram of cluster sizes p_s is monoexponential

$$p_s \propto e^{-s/\tilde{s}} \tag{4}$$

and presented in Figure 12. The typical cluster size, $\tilde{s}$, decreases slowly with temperature, in agreement with the expectation that larger clusters disappear at high temperature (Figure 13).

For $T < T^*$, a percolating cluster appears, corresponding to a "peak", while the distribution of the remaining small clusters stays monoexponential, with a smaller $\tilde{s}$ (since the total number of particles is constant). We mention that the size p_* of the percolated cluster can be calculated from the distribution with the help of the total number of particles N . To be specific,

$$p_* = N - p_1 e^{1/\tilde{s}}(1 - e^{-[1+\tilde{s}\ln p_1]/\tilde{s}})/(e^{1/\tilde{s}} - 1) \approx N - p_1 e^{1/\tilde{s}}/(e^{1/\tilde{s}} - 1)$$

where p_1 is the number of individual particles and $[x]$ denotes the integer part of x.

E. Elastic Response. We further study the elastic response of the networks and the dependence of the shear modulus on the state of the system. We impose a shear deformation by (i) moving

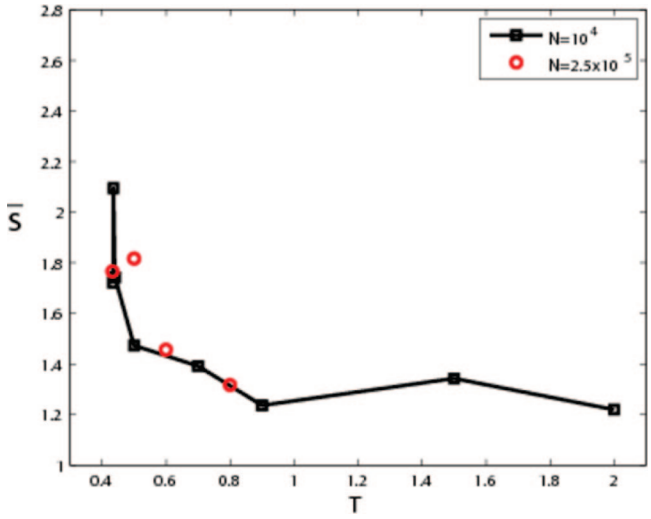

Figure 13. Mean cluster size $\bar{s}$ vs temperature T (square lattice, $k = 0.1$).

particles assigned to belong to the shear boundary layers ("wall") at a constant speed and (ii) by adding so-called Weeks−Chandler−Anderson (WCA) forces[16] (corresponding to just the repulsive part of the LJ potential) which are perpendicular to the walls and whose strength depends on the particle−wall distance. Moreover, we (iii) use periodic boundary conditions parallel to the walls and (iv) control temperature as for the equilibrium situation except that peculiar velocities (mismatch between absolute velocity and mean macroscopic velocity at the position of the particle) rather than absolute velocities are used.[17] The deformation is specified to grow linear in time until a certain prescribed maximum value, usually 0.5 (displacement at the boundary divided by box size), is reached. All results shown here have been obtained by starting from the ideal grid, i.e., from the homogeneous, "high-temperature" phase. Systems have been equilibrated before imposing a deformation. The presence of walls has an effect on the filamentous structure, as we will see, and results depend on the system size (this is the case for a pure LJ system, too[18]). The fixed lateral distance between particles in the wall layer prevents the formation of a HDP inside the wall and effectively repels these structures.

The first step was to check how boundary conditions and confinement affect the equilibrium properties of the network, in the absence of shear. For this purpose we investigated systems with two and also four walls. We find (not shown) that our order parameter ϕ possesses a slightly lower value in the confined situation. A more noticeable difference appears in the steady-state patterns just below T^* where circularly shaped filaments near the boundary replace the linear ones observed in the completely periodic systems. The circular shape arises when both ends of a growing linear filament approach a wall, change their growth direction, move along the walls, and eventually coalesce (see movie C from our add-on material[19]). Once a circular filament is formed, it is spreading toward the walls. This effect is enhanced if we insert four walls, as we have also tested. This phenomenon reminds one of the *Casimir* effect arising due to the fact that the filament divides the box into two domains; if the domains differ in size, the phonon pressure (due to thermal flucutations of the network in the low-density phase) in the larger domain "pushes" the filament toward the walls.

In a next step the system was subjected to a large-amplitude shear deformation, at a low shear rate which allows us estimate the (low frequency) shear modulus. The effect of shear deformation on the microphase-separated network is shown in Figure 14. The value of ϕ after applying the strain is found to be ~0.5 above its equilibrium value, and the transition at T^* is smooth

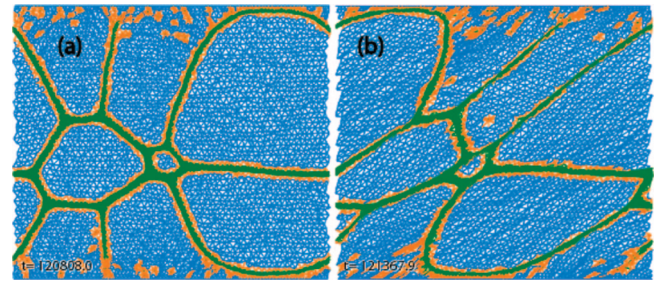

Figure 14. (a) Undeformed and (b) deformed (0.5 shear strain) state of the elastic LJ system with two walls ($N = 10\,000$, $k = 1/15$, $T = 0.25$, simulation started from hexagonal lattice, snapshots taken after 15M steps, corresponding shear rate $\dot{\gamma} = 4.17 \times 10^{-6}$ LJu); the images report times in LJ units, shear gradient in vertical direction).

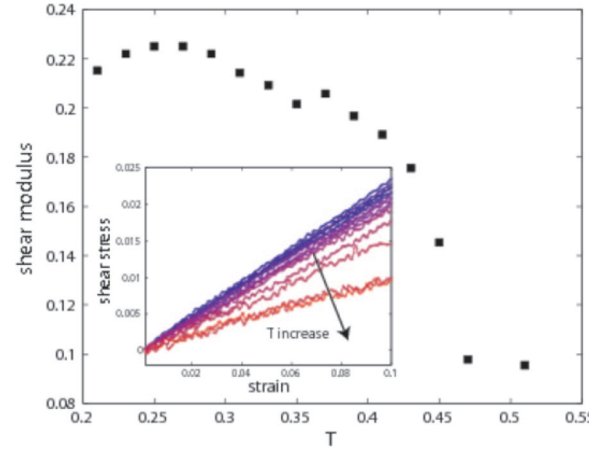

Figure 15. Shear modulus for the elastic LJ system with two walls ($N = 10\,000$, $k = 1/15$, $T = 0.33$); cf. Figure 14. The inset shows shear stress vs deformation, i.e., data from which the shear modulus had been extracted.

compared with the one observed in the undeformed situation (not shown). The shear modulus is one of several quantities for measuring the strength of materials. It is directly computed from the shear (xy-) component of the stress tensor $\boldsymbol{\sigma}$, which we measure instantaneously from positions and forces using the tensorial virial formula.[17,20] The microscopic expression reads

$$\boldsymbol{\sigma} = -\frac{1}{V}\left(\sum_{i=1}^{N} \mathbf{c}_i\mathbf{c}_i + \frac{1}{2}\sum_{i=1}^{N}\sum_{j=1}^{N} \mathbf{r}_{ij}\mathbf{F}_{ij}\right) \tag{5}$$

where $\mathbf{r}_{ij} \equiv \mathbf{r}_i - \mathbf{r}_j$, $\mathbf{F}_{ij} \equiv \mathbf{F}_i - \mathbf{F}_j$, and $\mathbf{F}_i$ denotes the total force vector on particle i (including contributions from walls, springs, LJ interactions). The kinetic part of the stress, first term in (5), contains peculiar velocities; here $\mathbf{c}_i = \mathbf{v}_i - \dot{\gamma}\mathbf{r}_i \cdot \mathbf{e}_x\mathbf{e}_y$ for the case of simple shear flow in x-direction, flow gradient in y-direction, with shear rate $\dot{\gamma}$, shear strain $\dot{\gamma}t$, where t is the time after cessation of deformation. Expressions for the elastic modulus tensor and the Voigt elastic moduli, relevant for anisotropic materials, have been presented and discussed for WCA fluids in ref 21. Values for the shear stress $\sigma \equiv \mathbf{e}_x \cdot \boldsymbol{\sigma} \cdot \mathbf{e}_y$ are extracted every 40 integration time steps. The shear modulus is calculated from the slope in the representation σ vs time. In Figure 15, we plot the shear modulus vs T for systems with two walls. A mechanical transition in the shear modulus is observed at $T \approx 0.45$ (see Figure 15). Below this temperature the modulus increases dramatically with decreasing T, i.e., with increasing order parameter, due to the increasing amount of rigid PHDC. We do not report error bars in Figure 15 because the data had been obtained by shearing a single equilibrated configuration, however independently generated for each temperature.

IV. Conclusions and Outlook

Recently,[13] we introduced a simple model of a network that contains two of the basic physical attributes of polymer gels: elastic restoring forces that oppose stretching of the chains between cross-links and attractive forces that promote segregation. The competition between these effects leads to microphase separation, in the course of which cellular structures composed of dense linear filaments surrounding low-density domains are formed. In the present paper we report an in-depth study of this model. We constructed a phase diagram and showed that microphase separation takes place in a broad range of spring constants. Below k_{min} the connectivity and elasticity of the network become irrelevant, and the system exhibits the characteristic phase separation behavior of a Lennard-Jones (LJ) fluid—a single spherical droplet of the dense phase is formed. Above k_{min}, the "macroscopic" droplet configuration gives way to microstructure that consists of (roughly spherical) dense clusters connected by stretched springs. At yet higher spring constant values a network of dense linear filaments connected by 3-fold vertices appears. Finally, above k_{max}, elastic restoring forces dominate over LJ attractions and phase separation is suppressed. We would like to emphasize that the microphase separation observed in our simulations is not put in by hand by introducing a molecular length scale into an effective free energy, the way it is done, for example, in models of diblock copolymers.[22] Furthermore, since our model has no topological entanglements, the mechanism of microphase separation differs from that predicted for segregation of interpenetrating polymer networks.[23]

Since the existence of the filamentous phase is a new important prediction of our model, in this work we focused on the properties of this phase. When the system is cooled below some temperature T^*, it undergoes microphase separation, and a percolating network of dense filaments connected by 3-fold vertices is formed. The width of these filaments is a weakly decreasing function of temperature but does not depend on the size of the system (compare the widths for the N = 10 000 and 250 000 particle systems in Figure 6 of ref 13). At T^* the characteristic length of a filament approaches the size of the system, but as the temperature is lowered it rapidly decreases as more and more filaments are formed. The cell dimensions decrease with the distance from the transition temperature, roughly as $(T^* - T)^{-\nu}$ (there is no divergence for finite system size!) where the exponent ν is close to 0.5. Although this value coincides with the mean-field correlation length exponent of the Ising model, the significance of this observation is unclear.

Notice that since macroscopic shrinking is prohibited by the fixed area constraint the network can only undergo microphase separation, and some sort of a modulated structure is thus expected to appear in thermal equilibrium. Therefore, the observation of cellular patterns is insufficient to establish whether they are equilibrium or kinetically frozen metastable structures (akin to the spongelike patterns that appear in a phenomenological model of the volume phase transition in a gel[7,8]).

The evidence concerning the question of equilibrium is inconclusive. For example, as temperature is lowered, thermal fluctuations play a progressively smaller role, and the system should approach its ground-state (lowest energy) configuration. Normally, such a ground state is nondegenerate and possesses a high degree of symmetry. However, this is not always the case; for example, an Ising antiferromagnet on a triangular lattice has a highly degenerate ground state, and therefore its entropy remains finite in the limit of zero temperature.[24] Indeed, in our case, lowering the temperature below T^* yields one particular realization of a large set of disordered configurations, each of which is characterized by the same order parameter and average domain size (see two such realizations of the steady-state patterns for the same simulation parameters at Figure 16). Thus, it is possible that in our system as well frustration due to the presence of the elastic springs leads to a degenerate ground state and that small variation of initial conditions may lead to microscopically different ground states (with the same macroscopic properties). Alternatively, one may conclude that the steady state in which cellular structures are observed corresponds to late stage nucleation of the new phase, whose growth and coarsening are arrested by the elastic stresses that develop in the stretched network. Indeed, the filaments appear to grow by absorbing small clusters that appear immediately following the quench to a lower temperature, a phenomenon resembling the Lifshitz–Slyozov mechanism of coarsening by droplet coalescence. Closer inspection reveals that the analogy with classical nucleation is limited. If the number of filaments would be determined by the probability of their nucleation rather than by equilibrium considerations, one would expect this number to increase linearly with the total area of the system. Contrary to this expectation, we find that a single filament (or one that closes on itself due to periodic boundary conditions, thus forming a hexagonal cell) always appears in the simulation box, just below the transition temperature, *independent of system size*.

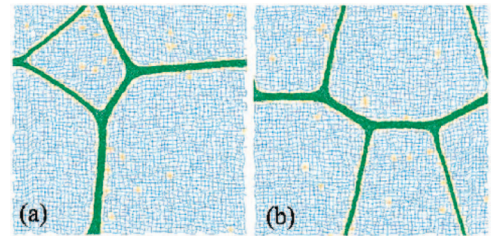

Figure 16. Two typical steady-state patterns observed at $T = 0.32$ ($k = 0.1$, $N = 10\,000$, relaxed from the initial square grid), obtained by using different initial velocities of the particles. Each of the configurations is characterized by the same order parameter and average domain size.

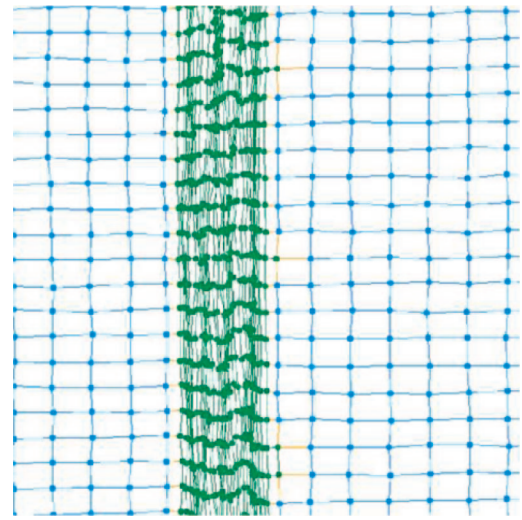

Figure 17. Close-up view of the time-averaged configuration of a system with parameters $N = 10\,000$, $k = 0.1$, and $T = 0.4$.

While it is clear that the formation of filaments is a consequence of the interplay between attractive and elastic forces in the network, we were not able to come up with a simple analytical model in which the shape of high density clusters is determined by minimization of elastic energy (the way the spherical shape of a liquid droplet minimizes its surface energy). Nevertheless, important insights can be obtained by examining the time-averaged configurations of the network after steady state has been reached. Inspection of Figure 17 reveals that the filament is assembled by a folding process in which neighboring parallel lines of particles are brought together sequentially. Examination of the low-density phase surrounding the filament shows that springs

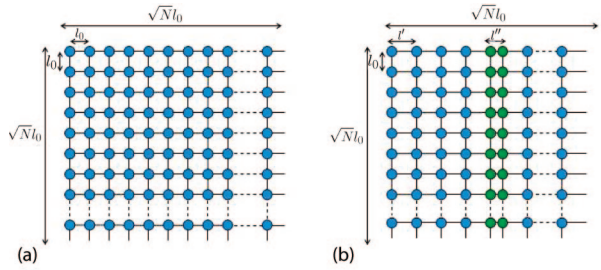

Figure 18. Schematic view of the simple cubic lattice. Lines and nodes represent springs and LJ particles, respectively. In (a) we show the initial state and in (b) the assumed lowest energy elastic deformation mode.

parallel to the axis of the filament are nearly undeformed while those perpendicular to it are stretched. This agrees with the expectation that the formation of the high-density phase proceeds through coupling to the lowest energy modes that correspond to one-dimensional, uniform deformation of the elastic network. Presumably, further assembly (and thus further thickening of the filament) stops when the stretching of the springs that remain in the low-density phase balances the attractive LJ forces.

At this point we would like to comment on the generality of our results. All the results were obtained for a given set of parameters (lattice topology, system size, density, spring constant, and initial configuration). In order to test the generality of our results, we performed a set of simulations in which these parameters were varied. We find that when the square lattice is replaced by a hexagonal one (and the spring constant is reduced from $k = 1/10$ to $k = 1/15$ to compensate for the increased coordination number such that the total elastic energy of the initial configuration is the same for both lattices) or when the number of particles is changed from N = 10 000 to N = 250 000, all our qualitative conclusions concerning the phase separation remain unaffected. The sensitivity of the results to the initial conditions was tested by applying random spring coefficients (we chose a uniform random distribution in a symmetric interval about some typical k)[13] and by starting from an inhomogeneous "droplet" configuration, instead of placing the particles on an ideal lattice.[25] Again, in both cases, the qualitative results remain unaffected.

Future studies based on our simple model can take several directions. An obvious extension involves the study of phase separation in 3D networks. Even though we expect the system to form a bicontinuous phase at low temperatures, with dense domains embedded in a dilute, stretched network, we do not know whether the dense clusters will consist of linear filaments connected into a network-like structure as in 2D or will combine into a soaplike structure made of connected surfaces (the latter possibility is favored by the 1D character of the lowest energy elastic deformation model; see Figure 18). Another possible direction involves incorporation of real attributes of polymer networks such as the random distribution of cross-links and examination of their effect on the microphase separation patterns. Finally, in order to attempt to connect the simulation to analytical results, one may study phase separation in one-dimensional networks, for which approximate analytical treatments can be constructed and physical quantities such as the entropy and the distributions of dense clusters can be calculated. We are pursuing these directions at the present time.

Appendix A. Estimating Bound for Spring Coefficient

In the undeformed state (Figure 18a), all the springs are of length l_0 and the potential energy is

$$E_a = \frac{1}{2}kl_0{}^2 2N$$

In this state there is no contribution of the LJ potential, since $l_0 < r_{cut}$. However, in the deformed state (Figure 18b), the length of the springs along the x-axis converts from l_0 to l' and $l'' < r_{cut}$, and the potential energy is composed of the LJ and the elastic contributions:

$$E_b = \frac{1}{2}kl_0{}^2 N + \frac{1}{2}kl'^2(N - \sqrt{N}) + \frac{1}{2}kl''^2\sqrt{N} - \epsilon\sqrt{N}$$

where $\epsilon = -U_{LJ}(l'')$. Since the total area is conserved, $l'(\sqrt{N} - 1) + l'' = l_0\sqrt{N}$. Thus, for $N \gg 1$

$$\begin{aligned} l' &= \frac{l_0\sqrt{N} - l''}{\sqrt{N} - 1} = l_0 \frac{1 - l''/(l_0\sqrt{N})}{1 - 1/\sqrt{N}} \\ &\approx l_0(1 - l''/(l_0\sqrt{N}))(1 + 1/\sqrt{N}) \\ &\approx l_0\left(1 + \frac{1 - l''/l_0}{\sqrt{N}}\right) \end{aligned}$$

Next, we equate $E_a(k_{max}) = E_b(k_{max})$ and conclude

$$k_{max} = \frac{2\epsilon}{(l_0 - l'')^2}$$

which yields at $k_{max} \approx 0.31$ for the present simulations, where $l_0 = 3.5$, $l'' \approx 1.25$ for temperatures well below T^*, and $\epsilon = -U_{LJ}(l'') \approx 0.77$.

Appendix B. Algorithms

Algorithm 1 Maintain constant temperature.

$E_{KIN} \Leftarrow 0$
for $i = 1$ to N **do**
  $E_{KIN} \Leftarrow E_{KIN} + \sqrt{v[i]_x^2 + v[i]_y^2}$
end for
for $i = 1$ to N **do**
  $v[i]_x \Leftarrow v[i]_x \times \sqrt{T/E_{KIN}}$
  $v[i]_y \Leftarrow v[i]_y \times \sqrt{T/E_{KIN}}$
end for

Algorithm 2 Maintain the PBC.

for $i = 1$ to N **do**
  $r[i]_x \Leftarrow r[i]_x - \text{round}(r[i]_x/L_x) \times L_x$
  $r[i]_y \Leftarrow r[i]_y - \text{round}(r[i]_y/L_y) \times L_y$
  // round(x) rounds x to its nearest integer //
end for

Algorithm 3 Calculate E_{SP} with the PBC.

$E_{SP} \Leftarrow 0$
for $i = 1$ to N **do**
  for $j = 1$ to ζ **do**
    neighbor$\Leftarrow j$
    $dr.x \Leftarrow r[i]_x - r[\text{neighbor}]_x$
    $dr[i]_x \Leftarrow dr[i]_x - \text{round}(dr[i]_x/L_x) \times L_x$
    $dr_y \Leftarrow r[i]_y - r[\text{neighbor}]_y$
    $dr[i]_y \Leftarrow dr[i]_y - \text{round}(dr[i]_y/L_y) \times L_y$
    $E_{SP} \Leftarrow E_{SP} + \sqrt{dr[i]_x^2 + dr[i]_y^2}$
  end for
end for

Algorithm 4 Obtain a density matrix.

$C[i, j, t] \Leftarrow \text{medfilt2}(C[i, j, t], [5, 5])$;
// medfilt2(A,[m,n]) performs median filtering of the matrix A in two dimensions. Each output pixel contains the median value in the m-by-n neighborhood around the corresponding pixel in the input image. The command pads the image with zeros on the edges, so the median values for the points within [m n]/2 of the edges may appear distorted //

References and Notes

(1) Onuki, A. *Adv. Polym. Sci.* **1993**, *109*, 63.
(2) Panyukov, S. V.; Rabin, Y. *Macromolecules* **1996**, *29*, 8530.
(3) Plischke, M. Bergersen, B. *Equilibrium Statistical Physics*, 3rd ed.; World Scientific: Singapore, 2006; p 112.
(4) Hashimoto, T. *Phase Transitions* **1988**, *12*, 47.
(5) Chaikin, P. M.; Chaikin, P. M.; Lubensky, T. C. *Principles of Condensed Matter Physics*; Cambridge University Press: Cambridge,

1995.
(6) Gunton, J. D.; San Miguel, M. P.; Sahni, S. In *Phase Transitions and Critical Phenomena*; Lebowitz, J. L., Ed.; Academic Press: London, 1983; Vol. 8, p 267.
(7) Onuki, A.; Puri, S. *Phys. Rev. E* **1999**, *59*, 1331.
(8) Sekimoto, K.; Suematsu, N.; Kawasaki, K. *Phys. Rev. A* **1989**, *39*, 4912.
(9) Flory, P. J. *Principles of Polymer Chemistry*; Cornell University Press: Ithaca, NY, 1953.
(10) Rapaport, D. *The Art of Molecular Dynamics Simulation*, 2nd ed.; Cambridge University Press: Cambridge, 2004.
(11) Reduced units—online interactive tool.
(12) Kröger, M. *Models for Polymeric and Anisotropic Liquids*; Springer: Berlin, 2005.
(13) Peleg, O.; Kröger, M.; Hecht, I.; Rabin, Y. *EPL* **2007**, *77*, 58007.
(14) Cormen, T. H.; Leiserson, C. E.; Rivest, R. L.; Stein, C. *Introduction to Algorithms*, 2nd ed.; MIT Press: Cambridge, MA, 2003.
(15) Boccalettia, S.; Latorab, V.; Morenod, Y.; Chavezf, M.; Hwanga, D.-U. *Phys. Rep.* **2006**, *424*, 175.
(16) Hess, S.; Kröger, M.; Voigt, H. *Physica A* **1998**, *250*, 58.
(17) Kröger, M.; Loose, W.; Hess, S. *J. Rheol.* **1993**, *37*, 1057.
(18) Schoen, M.; Diestler, D. J.; Cushman, J. H. *J. Chem. Phys.* **1987**, *87*, 5464.
(19) Movies and an interactive tool converting between reduced and dimensional units is permanently available at http://www.complexfluids.ethz.ch/gels.
(20) Frenkel, D.; Smit, B. *Understanding Molecular Simulation: From Algorithms to Applications*; Academic Press: London, 2002.
(21) Hess, S.; Kröger, M.; Hoover, W. G. *Physica A* **1997**, *239*, 449.
(22) Leibler, L. *Macromolecules* **1980**, *13*, 1602.
(23) Frisch, H. L.; Grosberg, A. Y. *Makromol. Chem. Theory Simul.* **1993**, *2*, 517.
(24) Wannier, G. H. *Phys. Rev.* **1950**, *79*, 357.
(25) Kröger, M.; Peleg, O.; Ding, Y.; Rabin, Y. *Soft Matter* **2008**, *4*, 18..

MA702732T